GEOPHYSICS®

Radius Estimation of Subsurface Cylindrical Object from GPR Data using Full-waveform Inversion

Journal:	*Geophysics*
Manuscript ID	GEO-2017-0815.R1
Manuscript Type:	Technical Paper
Keywords:	ground-penetrating radar (GPR), full-waveform inversion, 3D, wavelet, near surface
Area of Expertise:	Ground-Penetrating Radar, Engineering and Environmental Geophysics

RADIUS ESTIMATION OF SUBSURFACE CYLINDRICAL OBJECT FROM GPR DATA USING FULL-WAVEFORM INVERSION

RUNNING HEAD : GPR FWI FOR CYLINDER RADIUS ESTIMATION

Tao Liu[1,2,3], Anja Klotzsche[1,3], Mukund Pondkule[1,3], Harry Vereecken[1,3], Yi Su, and Jan van der Kruk[1,3]

[1] IBG-3: Agrosphere, Institute of Bio- and Geosciences, Forschungszentrum Jülich (FZJ), 52428 Jülich, Germany

[2] School of Electronic Science and Engineering, National University of Defense Technology (NUDT), Changsha 410073, China

[3] Centre for High-Performance Scientific Computing in Terrestrial Systems (TerrSys), 52428 Jülich, Germany

ta.liu@fz-juelich.de, a.klotzsche@fz-juelich.de, m.pondkule@fz-juelich.de, h.vereecken@fz-juelich.de, y.su@yeah.net, j.van.der.kruk@fz-juelich.de

Original paper date of submission: Dec.16, 2017

Revised paper date of submission: Mar. 7, 2018

Accepted on: Jul. 5, 2018

ABSTRACT

Ray-based radius estimation of subsurface cylindrical objects like rebars and pipes from ground penetrating radar (GPR) measurements are not accurate because of their approximations. Here, we present a novel full-waveform inversion (FWI) approach that uses a full-waveform 3D FDTD forward modeling program to estimate the radius including other object parameters. By using the full-waveform of the common-offset GPR data, the Shuffled Complex Evolution (SCE) approach is able to reliably extract the radius of the subsurface cylindrical objects. A combined optimization of radius, medium properties and the effective source wavelet is necessary. Synthetic and experimental data inversion returns an accurate reconstruction of the cylinder properties, medium properties, and the effective source wavelet. Combining FWI of GPR data using SCE and a 3D FDTD forward model makes the approach easily adaptable for a wide range of other GPR FWI approaches.

INTRODUCTION

Ground Penetrating Radar (GPR) is widely used in geophysical, environmental, and civil engineering applications as a quick and efficient non-destructive exploration technique. The information contained in GPR signal, such as the travel time, waveform, and amplitude, enable several approaches to non-invasively investigate and/or monitor underground infrastructure, concrete, bridge decks, and roads. For instance, information on the ice-layer thickness variation important for the security of winter roads was obtained by Annan et al. (2016). The direct ground wave was used for the on-site physical characterization of moisture and chloride content of concrete (Sbartaï et al., 2006; Sbartaï et al., 2012), and the temporal spectral absorption of GPR signals can be related to water content in brick walls (Wai-Lok Lai et al., 2014). Dérobert et al.

(2008) and Ihamouten et al. (2011) combined a capacitive technique with GPR for the non-destructive evaluation of cover concrete and hydraulic concrete. Zanzi et al. (2013) explored the use of dual-polarized GPR data to estimate rebar diameters, and Hong et al. (2017) performed a long-term monitoring of reinforcement corrosion using the GPR signal attenuation.

Among these applications, the detection and characterization of subsurface cylindrical objects (location, depth, and diameter) are of high interest since the cylindrical objects can be related to a wide variety of subsurface infrastructures such as pipelines, cylindrical tanks, cables, and rebars, which are critical for maintenance and securing complex urban facilities. With a common-offset GPR measurement, the radargrams measured over cylindrical objects return a distinct hyperbolic feature that depends on the geometrical structure and dielectric properties of the subsurface and the object. Based on this hyperbolic features, the detection and localization of the subsurface cylindrical objects have been well studied using several approaches such as the Hough transform, neural network, template matching, etc. (Caorsi and Cevini, 2005; Shihab and Al-Nuaimy, 2005; Windsor et al., 2005; Pasolli et al., 2009; Kaur et al., 2016). Several automatic analysis approaches are developed, for example, Soldovieri et al. (2011) presented an improved imaging technique for the detection of rebars based on a minimization algorithm taking the advantage of the sparseness assumption, and Kaur et al. (2016) developed an automated rebar analysis for robotic bridge deck evaluation based on machine learning classification and curve fitting.

Whereas the location and depth of a cylindrical object can be relatively easy extracted from a hyperbola, to extract the diameter with GPR is more challenging. The main difficulty is that the radius, depth, and wave velocity information within a hyperbolic pattern over cylindrical

object can be strongly correlated, e.g. for a larger radius pipe a flatter hyperbole will be measured similar to when the velocity is increasing (Borgioli et al., 2008; Ristic et al., 2009). By high frequency assuming that the propagation and the scattering of electromagnetic wave are of physical optics behavior, ray-based methods using a geometrical analysis were explored. Windsor et al. (2005) estimated the radius from GPR data by using the Hough transform (HT), while Borgioli et al. (2008) developed a weighted HT method and improved the performance for multiple hyperbolas. However, in these approaches the velocity should be already known or estimated beforehand. Shihab et al. (2005) and Ristic et al. (2009) investigated and developed a hyperbola fitting method for zero-offset measurements, where the hyperbola signature over a cylindrical object was derived as a function of the radius, depth and wave velocity, which was fitted with the picked observed hyperbola traveltimes. These approaches were promising, but also indicated the difficulties caused by the strong correlation of the parameters for real measured data. By picking the highest reflected intensity from the hyperbolic patterns (manually or automatically), additional errors for the travel time are introduced, and consequently increased the radius estimation error (Borgioli et al., 2008).

A possible approach that does not include so many approximations is to perform a full-waveform inversion of the measured hyperbolic data using a detailed forward model instead of using picked travel times and an approximated forward model. By using the full waveform of the measured data and optimizing the medium properties with an advanced forward model, which can explain the full-waveform of the measured data, enables the use of less approximations and more reliable results can be obtained. Full-waveform inversion approaches have been initially developed for seismic data and in recent years several FWI approaches have been developed for GPR. First GPR FWI approaches using a gradient-based minimization were implemented for

crosshole GPR by Ernst et al. (2007a, 2007b) and Kuroda et al. (2007), who introduced the FWI scheme using a 2D finite-difference time-domain (FDTD) solution of Maxwell's equations. Meles et al. (2010) improved this method by including the vector properties of the electric field. For the FWI of measured GPR data, it is important to also estimate an effective wavelet (Ernst et al., 2007a) since this is unknown and often depends on the coupling of the source and receiver antennas. Usually, one effective wavelet is estimated for one crosshole measurement gather. Klotzsche et al. (2010) applied this approach to experimental borehole GPR data and characterized a low-velocity waveguide structure (Klotzsche et al., 2012) and high porosity layer (Klotzsche et al., 2014) in a gravel aquifer. Recently, Gueting et al. (2017) implemented a high resolution large-scale aquifer characterization using crosshole GPR full-waveform tomography. Gloaguen et al. (2007) developed a pseudo-full-waveform inversion of borehole GPR data using stochastic tomography, whereas Cordua et al. (2012) present a general Monte Carlo full-waveform inversion strategy that integrates a priori information described by geostatistical algorithms with Bayesian inverse problem theory. Babcock and Bradford (2015) implemented the GPR waveform inversion for quantifying properties for nonaqueous phase liquid thin and ultrathin layers, and Bradford et al. (2016) used a targeted GPR reflection-waveform inversion algorithm to quantify the geometry of oil spills under and within sea ice. Sassen and Everett (2009) combined the full-waveform inversion and the fully polarimetric GPR coherency technology to characterize the fractured rock, and Schmid et al. (2016) studied the application of FWI to deduce the snow stratigraphy from the upward-looking GPR data. Recently, Feng et al. (2017) developed a new approach for joint full-waveform inversion of crosshole seismic and GPR data to improve the inversion result.

For civil engineering applications, gradient-free FWI approaches have been implemented for off-ground GPR applications to estimate the chloride and moisture content in concrete (Kalogeropoulos et al., 2011) and to assess chloride gradients in concrete (Kalogeropoulos et al., 2013). Since the antenna is present in air, the source wavelet does not depend on the medium properties and an effective source wavelet can be estimated prior to the FWI of the data, using a calibration measurement above a metal plate.

For surface GPR applications, the emitted and received wavelet is depending on the medium properties of the sensed material parameters due to the coupling of the source and receiver antennas. For increasing permittivity, the wavelets center frequency decreases, whereas the wavelets amplitude increases, which is consistent with the radiation pattern and the antenna coupling characteristics (Busch et al., 2014). Since the wavelet is coupled with the medium properties, an independent wavelet estimation followed by FWI is not possible and the effective wavelet needs to be jointly estimated with the medium properties. Busch et al. (2012) successfully used a combined sequential inversion of model and source wavelet followed by simultaneous model optimization to invert the ground wave and waveguide layer reflections (Busch et al., 2012) and improved the characterization of fine-texture soils (Busch et al., 2014).

To reliably estimate the radius and other parameters for a subsurface cylindrical object, here, we introduce a novel radius estimation approach by adapting the frequency-domain FWI for surface GPR data. This work uses the combined sequential and simultaneous optimization of both the model and source wavelet (Busch et al., 2012), in which the forward modeling is performed by the FDTD electromagnetic simulation tool gprMax3D (Giannopoulos, 2005; Warren et al., 2016), and the effective source wavelet is accomplished by the deconvolution

method (Busch et al., 2012). Note that a classical 2D simplification would not accurately describe the geometrical spreading of electromagnetic wave present in a real 3D world, since the commonly used 3D to 2D conversion introduce approximation errors (Busch et al., 2012).

Using a versatile 3D forward modeling approach enables the inclusion of all the vector propagation effects including radiation patterns and geometrical spreading, such that no approximations need to be introduced. The Shuffled Complex Evolution (SCE) (Duan et al., 1993), a robust and model independent global optimization approach, is employed to optimize the model parameters, which can avoid the inversion being trapped in a local minimum such that an improved global minimum can be found. A hybrid MPI+OpenMP parallel computing architecture has been implemented to accelerate the inversion and to have an acceptable calculation time (Krause and Thörnig, 2016). Inversion of synthetic reflection data of an air-filled plastic pipe and measured data from a water-filled pipe prove the validity of the new method.

GPR COMMON-OFFSET MEASUREMENT OF SUBSURFACE CYLINDRICAL OBJECT

Figure 1 shows a schematic setup of a common-offset GPR measurement over a subsurface cylindrical object extending in the y-direction. The positions of the antenna center are indicated by x_i whereas x_0 shows the position above the center of the cylinder. The subsurface medium is described as a homogeneous half-space, which is described by the relative permittivity ε_r and conductivity σ. R and d stand for the radius and center depth of the cylinder, respectively. The magnetic permeability is set to μ_0.

With the GPR moving across the subsurface cylindrical object along the surface's *x*-direction, a common-offset B-scan is obtained. The pipe parameters can be changed such that an air-filled, water-filled tube, rebar or else can be modeled.

RAY-BASED ANALYSIS

The classical ray-based approach uses the far-field assumption and simplifies the propagation and scattering of electromagnetic waves. In addition, a zero offset configuration is often assumed where source and receiver are present at the same position (Borgioli et al., 2008).

By assuming that the reflection occurs on the line between the antenna center and the cylinder's axis, and introducing the cylindrical radius R, the range distance r_i, and x_0 as the horizontal position of the subsurface cylinder that can be determined using the vertex of the hyperbola in the B-scan data, the distance between the measurement point and the center of the cylinder equals

$$r_i + R = \sqrt{(x_i - x_0)^2 + (r_0 + R)^2}\ , \tag{1}$$

where r_0 is the distance between the top of the cylindrical object and the surface, x_i is the measurement position, and x_0 indicates the position above the center of the cylinder. Then the corresponding two-way travel time t_i can be expressed approximately by

$$t_i \approx \frac{2}{v}\left(\sqrt{\left(\frac{vt_0}{2} + R\right)^2 + (x_i - x_0)^2} - R\right), \tag{2}$$

in which v is the wave velocity in the medium and t_0 is the two-way travel time corresponding to the antenna location that is on top of the cylinder.

The relation between the travel time, the radius, and the velocity in equation 2 can be rewritten as the classical hyperbola equation centered around (x_0, -2R/v) (Shihab and Al-Nuaimy, 2005):

$$\frac{\left(t_i + 2R/v\right)^2}{\left(t_0 + 2R/v\right)^2} - \frac{\left(x_i - x_0\right)^2}{\left(vt_0/2 + R\right)^2} = 1, \tag{3}$$

which show the dependency of the geometrical properties of the hyperbola with respect to R, t_0 and v. In theory, by fitting equation 3 with the (x_i, t_i) pairs extracted from the hyperbolic pattern in the common-offset B-scan data, the radius, depth and the wave velocity can be estimated.

Equation 3 on the other hand indicates that the effective radius estimation relies highly on the effectivity of the extracted hyperbola, i.e., if the extracted hyperbolic pattern is not accurate, then the estimated radius also contains error. Generally, when the dimension of the subsurface cylinder is large enough compared to the wavelength, the ray-based assumption can well approximate the behavior of wavefront (Borgioli et al., 2008). Nevertheless, diameter estimation with merely geometrical analysis fails when the wavelength is comparable or larger than the target (Zanzi and Arosio, 2013). The inevitable measurement uncertainties relating to zero time, position and travel time moreover cause stochastic errors to the estimated radius (Windsor et al., 2005; Ristic et al., 2009). For the target locating in the near-field zone of antenna, for instance the rebar under shallow concrete surface, the generally adopted far-field monostatic antenna model (Borgioli et al., 2008), antenna radiation pattern (Streich and van der Kruk, 2007; van der

Kruk et al., 2010) and the finite antenna length effect (Montoya and Smith, 1996), *etc*., can cause wave distortion and consequently introduce uncertainties to the radius estimation. Since the ray-based method is based on several approximations, the obtained radius may not agree with the true value.

To overcome several of these ray-based limitations, we propose to use an accurate forward model, that enables the use of the full waveform, the spreading effect of the electromagnetic field in 3D space, the attenuation of the medium and the radiation pattern of GPR dipole antennas. By using a FWI approach, all the information in the measurement can be included to return a reliable and quantitative estimation of the geometry of the subsurface cylindrical objects.

FULL-WAVEFORM INVERSION OF THE SUBSURFACE CYLINDRICAL OBJECT PARAMETERS

As an advanced data-fitting approach, the FWI scheme finds the model that explains best the measured data obtained from the scanning zone by minimizing the misfit between the observed and modeled data. An efficient and precise forward modeling tool is crucial, and a 2D approach would not accurately describe the geometrical spreading and antenna characteristics which are present in a real 3D measurement. Commonly used 3D to 2D conversion schemes also introduce approximation errors for surface GPR setups (Busch et al., 2012). Therefore, we use the 3D FDTD forward modeling tool gprMax3D, which is commonly used to model specific GPR setups and configurations (Giannopoulos, 2005; Warren et al., 2016). Since very detailed GPR measurements can be modeled in gprMax3D, this also enables the inclusion of more

complexity when necessary or to adapt this approach for the inversion of other subsurface objects.

To enable a coupling of the 3D forward model with our full-waveform inversion, we introduce a limited number of parameters that describe the properties of the system we want to estimate. The known parameters that stay constant during the inversion are the number of traces, the positions, and the offset between the source and receiver antennas. As unknown parameters used for the input of forward model we take ε_r, R, d, σ, and the effective source wavelet. Currently, the content in and the material of the subsurface cylindrical object are not included in the model yet and the unknown parameters for defining the model are expressed as $\mathbf{m} = [\varepsilon_r, \sigma, R, d]$.

Initial Source Wavelet Estimation

To invert experimental data, it is important to estimate the effective source wavelet since this is unknown for commercial GPR system and also depends on the coupling of the antennas. Whereas the electric field $E(t, \mathbf{x}, \mathbf{m})$ in time domain is a convolution of the source wavelet $W(t)$ with the Green's function $G(t, \mathbf{x}, \mathbf{m})$, it can be written as a multiplication in frequency domain as follows:

$$\hat{E}(f, \mathbf{x}, \mathbf{m}) = \hat{G}(f, \mathbf{x}, \mathbf{m}) \cdot \hat{W}(f) \tag{4}$$

where ^ indicates frequency domain.

As the 1st step of the inversion, initial starting parameters for ε_r, R, and d are estimated using the far-field ray-based method. Since the ray-based approach cannot estimate the conductivity, the initial σ can only be guessed.

Prior to calculating any misfit function that we want to optimize using a full-waveform inversion approach, we need to determine an effective source wavelet that serves as input in the forward modeling. Since any synthetic wavelet, like Ricker or Gaussian does not have enough degrees of freedom to enable the characterization of the true effective wavelet, here, we estimate an effective wavelet from the measured data itself by using a deconvolution technique (Ernst et al., 2007a; Kalogeropoulos et al., 2011; Busch et al., 2012).

First, synthetic data $\hat{E}(f_n, x_m, \mathbf{m})$ is calculated for a certain number of traces, which are used for the inversion, with the ray-based start values including the initial σ. A synthetic source wavelet $\hat{W}(f_n)$ is used as input for the modeling, that is subsequently removed from the $\hat{E}(f_n, x_m, \mathbf{m})$ by a deconvolution. In this way, the Green's function $\hat{G}(f_n, x_m, \mathbf{m})$ that describes all propagation effects in a 3D space is estimated for each frequency component and trace separately

$$\hat{G}(f_n, x_m, \mathbf{m}) = \hat{W}^{-1}(f_n) \cdot \hat{E}(f_n, x_m, \mathbf{m}) \tag{5}$$

Next, the observed GPR data $\hat{E}_{\text{obs}}(f_n, x_m, \mathbf{m})$ is deconvolved in a least-squares sense by the estimated Green's function as follows

$$\hat{W}_{\text{est}}(f_n) = \hat{G}^{-1}(f_n, x_m, \mathbf{m}) \cdot \hat{E}_{\text{obs}}(f_n, x_m, \mathbf{m}) \tag{6}$$

where $\hat{W}_{\text{est}}(f_n)$ is the estimated effective source wavelet.

As can be seen from equations 5 and 6, any error in the model parameters will be compensated by an error in the estimated source wavelet. For instance, a too high value for the conductivity will be compensated by an unusually large value for the wavelet amplitude, and vice versa. This implies that the model parameters and source wavelet are coupled and that for the FWI of measured data, both the wavelet and the model properties need to be estimated simultaneously (Busch et al., 2012).

Shuffled Complex Evolution (SCE) Optimization Strategy

To optimally search for the ε_r, R, d, σ, and, $\hat{W}_{\text{est}}(f_n)$ that explain best the measured data, an efficient optimization algorithm is needed. For off-ground FWI approaches, combined global local search approaches were used to invert concrete properties including chloride gradients (Kalogeropoulos et al., 2011; Kalogeropoulos et al., 2013), where it was important to use high-quality starting model parameters before adding more complexity to the model. Note that these approaches did not need an optimization of the effective source wavelet because the source wavelet did not depend on the medium properties considering that the source was present in the air and no coupling existed between the medium properties and the effective source wavelet.

Here, we use the Shuffled Complex Evolution (SCE) for the FWI, which is a model-independent global optimization strategy promising to be robust, effective, and efficient for a broad class of problems (Duan et al., 1993). As the SCE starts the optimization with a controlled random search, the dependence on the starting model is reduced. In addition, the usage of hybrid parallel computing makes the combination of SCE and detailed 3D forward modeling to be achievable (Krause and Thörnig, 2016).

Sequential Phase- and Amplitude optimization

To be able to optimize the effective wavelet parameters while optimizing the model properties, we introduce in addition phase and amplitude factor, φ and A, such that the source wavelet can be updated as follows (Busch et al., 2012):

$$\hat{W}'_{\text{est}}(f_n) = \hat{W}_{est}(f_n) \cdot A \cdot \exp(j\varphi) \tag{7}$$

Instead of optimizing for all parameters, [ε_r, R, d, σ, φ, A], at the same time, we split up the high dimensional search parameter space into two lower dimensional spaces, for efficiency purposes (Duan et al., 1993; Busch et al., 2012). In the frequency domain, the data's phase component is affected mostly by the phase of the source wavelet and the travel time which is determined by the wave velocity of the medium and the relative position between GPR and the target. Similarly, the frequency domain amplitude component is influenced mainly by the amplitude of the source wavelet and the attenuation property σ (Jol, 2008). Therefore, we introduce phase-parameters $\mathbf{m}_P = [\varepsilon_r, R, d, \varphi]$, and amplitude-parameters $\mathbf{m}_A = [\sigma, A]$ that are successively optimized by the SCE algorithm as indicated in Figure 2.

The cost function for phase-parameters optimization is expressed by C_P

$$C_P(\mathbf{m}_P^k) = \frac{1}{M \cdot N} \sum_{m=1}^{M} \sum_{n=1}^{N} \left(\left| \frac{\hat{E}_{\text{mod}}\left(f_n, x_m, \mathbf{m}_P^k\right)}{\left|\hat{E}_{\text{mod}}\left(f_n, x_m, \mathbf{m}_P^k\right)\right|} - \frac{\hat{E}_{\text{obs}}\left(f_n, x_m, \mathbf{m}\right)}{\left|\hat{E}_{\text{obs}}\left(f_n, x_m, \mathbf{m}\right)\right|} \right| \right) \tag{8}$$

where $\hat{E}_{\text{mod}}(f_n, x_m, \mathbf{m}_P^k)$ indicates the frequency domain forward-modeled data with the estimated effective source wavelet, whereas $\hat{E}_{\text{obs}}(f_n, x_m, \mathbf{m})$ is the observed (measured) data. M and N demonstrate the number of traces and frequency points in the inversion, and superscript k

indicates the iteration. By normalizing the amplitude of the data (see denominator in C_P described by equation 8), the SCE FWI minimizes the misfit of the phase components between the modeled and observed data. During the phase-parameter optimization (step 3), the amplitude parameters $\mathbf{m}_A^k$ keeps unchanged while the phase mismatch of the source wavelet is optimized through the phase factor φ. When the parameters combination $\mathbf{m}_P^k$ with the smallest misfit for C_P is obtained, the source wavelet is updated in step 4 (see Figure 2) using

$$\hat{W}_{\text{est}}^k = \hat{W}_{est}^k \cdot e^{j\varphi^k} \tag{9}$$

Note that after step 4, the effect of φ is already involved in the source wavelet, hence it is reset to 0.

In step 5, the amplitude parameters $\mathbf{m}_A = [\sigma, A]$ are optimized by minimizing cost function C_A

$$C_A(\mathbf{m}_A^k) = \frac{1}{M \cdot N} \sum_{m=1}^{M} \sum_{n=1}^{N} \left(\left| \frac{\left| \hat{E}_{\text{mod}}\left(f_n, x_m, \mathbf{m}_A^k\right) \right| - \left| \hat{E}_{\text{obs}}\left(f_n, x_m, \mathbf{m}\right) \right|}{\hat{E}^{\max}\left(x_m\right)} \right| \right) \tag{10}$$

Here, the amplitude components are normalized by the maximum spectral amplitude of each measured trace $\hat{E}^{\max}(x_m) = \max\ \{|\hat{E}_{\text{obs}}(f_n, x_m, \mathbf{m})|, n = 1, 2, ..., N\}$, whereas the phase parameters are fixed during the amplitude parameters optimization. The parameter combination $\mathbf{m}_A^k$ that returns the smallest value for the cost function C_A as well as the optimized $\mathbf{m}_P^k$ in step 4 are used in step 6 where the effective source wavelet is updated.

Next in step 7, the cost function C_{fx} is evaluated that is defined by

$$C_{fx}(\mathbf{m}^k) = \frac{1}{M \cdot N} \sum_{m=1}^{M} \sum_{n=1}^{N} C\left(f_n, x_m, \mathbf{m}^k\right) \tag{11}$$

with

$$C\left(f_n, x_m, \mathbf{m}^k\right) = \left| \frac{\hat{E}_{\mathrm{mod}}\left(f_n, x_m, \mathbf{m}^k\right) - \hat{E}_{\mathrm{obs}}\left(f_n, x_m, \mathbf{m}\right)}{\hat{E}^{\max}\left(x_m\right)} \right| \tag{12}$$

where $\mathbf{m}^k$ contains only the model parameters [ε_r, R, d, σ] of the k^{th} iteration. When the obtained misfit function $C_{fx}(\mathbf{m}^{\mathrm{k}}) < C_{fx}(\mathbf{m}^{k-1})$ and the maximum iteration number is not yet reached, steps 3-6 are performed again until $C_{fx}(\mathbf{m}^{\mathrm{k}}) > C_{fx}(\mathbf{m}^{k-1})$ or a maximum iteration number is reached.

Simultaneous Phase- and Amplitude optimization

Finally, in step 8 a final simultaneous full-waveform inversion of the parameters $\mathbf{m}_s$ = [ε_r, R, d, σ] with the cost function given by equation 11 is performed while the source wavelet remains fixed, such that any coupled dependence on the relative permittivity and the conductivity can be optimized (Busch et al., 2012).

Due to the reduction of the inversion parameters and introducing an iterative sequential inversion approach, where also the effective source wavelet is being optimized, the inversion is able to converge more efficiently to the global optimum. The final simultaneous inversion of all parameters deals with the possible coupling of permittivity and conductivity and improves the accuracy of the estimated parameters. Accordingly, this approach balances the computing cost and convergence performance while enabling an accurate estimation of the unknown parameters.

To enable a more quantitative evaluation of the misfits, the following frequency and offset misfit functions are introduced

$$C_f(f_n, \mathbf{m}^k) = \frac{1}{M}\sum_{m=1}^{M}\left|\frac{\hat{E}_{\mathrm{mod}}\left(f_n, x_m, \mathbf{m}^k\right) - \hat{E}_{\mathrm{obs}}\left(f_n, x_m, \mathbf{m}\right)}{\hat{E}^{\max}\left(x_m\right)}\right|, \tag{13}$$

$$C_x(x_m, \mathbf{m}^k) = \frac{1}{N}\sum_{n=1}^{N}\left|\frac{\hat{E}_{\mathrm{mod}}\left(f_n, x_m, \mathbf{m}^k\right) - \hat{E}_{\mathrm{obs}}\left(f_n, x_m, \mathbf{m}\right)}{\hat{E}^{\max}\left(x_m\right)}\right|, \tag{14}$$

that show the obtained misfits as function of the frequency and offset, respectively.

FULL-WAVEFORM INVERSION OF SYNTHETIC DATA

To test the combined sequential and simultaneous inversion approach, a typical concrete setup corresponding to the scenario as introduced in Figure 1 was considered for the synthetic test. The subsurface medium is assumed to be wet concrete with a relative permittivity of 6.69 and electrical conductivity of 10 mS/m. In the subsurface, an air-filled cylinder is present to simulate a plastic pipe whose radius and center depth are 8 cm and 20 cm, respectively. A Ricker wavelet with a center frequency of 1 GHz was used as a pulse for exciting the Hertzian dipole antenna in gprMax3D. Perfect Matched Layer (PML) absorption is used to prevent reflections at the boundaries. The transmitter-receiver separation is set to be 10 cm. The pipe is located about 1~2 wavelengths away from the antennas and its dimension is comparable to the wavelength (about 0.12m at center frequency). Figure 3 a) shows the synthetic common-offset B-scan data. Note that the direct air and ground waves are already muted. Multiple reflections can be observed in Figure 3 a) since the electromagnetic wave is transmitted into the air-filled cylinder where multiple reflections occur and are partly received by the receiver antenna. Six traces

indicated by the black dash lines in Figure 3 a) are used for the inversion. Figure 3b) shows the six traces that are aligned to the first maximum peak. When picking the first trough or first peak, different arrival time changes will be obtained which indicates that the wavelet signatures are changing and any picking using a certain threshold will include errors due to the changing wavelet. Note the stretching of the waveform for increasing position is visible by the blue and red triangles for troughs and peaks, respectively. Comparison of the picks with the zero-offset travel-times obtained from using equation 2 also shows that erroneous travel times are obtained, which indicate also additional errors when using the zero-offset equation.

The full-waveform inversion presented in this work, can deal with these changing reflection shape and phase since this can be modeled with gprMax3D and less approximations have to be made. Generally, a start model can be obtained by using the ray-based method so that the inversion can achieve convergence in fewer iterations and therefore saving computation time. Here, we choose a start model that is relatively far away from the real parameter values. The complete model setup, the inversion configuration as well as the inversion result can be found in Table 1.

Start values were randomly set between the upper and the lower bound of the corresponding search range to investigate the stability and convergence performance of the approach and are more than 10% away from the true parameters (3rd row in Table 1). For a poor initial model, only a poor initial wavelet can be obtained such that the corresponding reconstructed traces (blue lines in Figure 3 c) are not consistent in waveform and amplitude with the synthetic data (black lines). When performing the initial source wavelet estimation, the influence of the erroneous initial model parameters are partly compensated by an erroneous

initial estimated source wavelet, which can be observed in Figure 4 a), where the initial estimated source wavelet (blue line) differs a lot in shape compared with the synthetic one (black line). For increasing iterations, the estimated source wavelet approaches the synthetic wavelet and is very similar to the true synthetic wavelet at the end of the sequential inversion.

For a quantitative evaluation of the proposed method, we analyze the average, frequency- and offset-dependent misfit using the cost functions given by equations 11, 13 and 14, respectively. Figure 4 b), shows that for the initial model, the normalized average misfit evaluated with equation 11 equals 0.59. This relatively high value indicates an incorrect start model and initial source wavelet. The misfit in Figure 4 b) shows a slight increase at the 2nd iteration (from 0.14 to 0.15). This non-monotonicity is natural at the early iterations because the source wavelet is not stable yet. The controlled random sampling strategy used by SCE can in this way move away from the current search range temporally and continue searching for the global minimum. For this reason, a minimum number of iterations must be preserved. For increasing iterations where the model parameters and the source wavelet are sequentially optimized, the average misfit significantly decreases to 3.4×10^{-3} at the 8th iteration where the convergence criterion is reached. After the final simultaneous inversion for $\mathbf{m}_s = [\varepsilon_r, R, d, \sigma]$, the misfit decreases further to 7.7×10^{-4}. Figure 4 c) and d) show the misfit cost functions C_f (equation 13) and C_x (equation 14), respectively.

Figure 3 c) and d) show that the modeled data for the inversion results and optimized effective source wavelet that is indicated by the red dash lines in time and frequency domain overlay the synthetic traces represented by the black lines, suggesting that the inversion results well explain the observed data. Note that the multiples in the modeled data in Figure 3 c) also

agree very well with the synthetic data and that the effective source wavelet is as well very close to the true wavelet shown in Figure 4 a).

The final inversion result, listed in the 5th row of Table 1, was obtained after 8 sequential optimization iterations and one final simultaneous optimization. The inversion provides an accurate estimation of the radius, depth, and permittivity with misfit lower than 1%, while the misfit for conductivity is slightly higher but still less than 2%.

Figure 5 shows the evolution of all parameters in which the parameters evolve towards the true values (marked by the red dash line) for increasing iteration. Although the inversion starts with a poor initial source wavelet, the permittivity, radius and center depth are still able to converge towards the true value due to the introduction of the phase-factor φ, which maintains stable after 5 iterations. In contrast, the evolution of conductivity shows more fluctuation because the variation of the electric field is more sensitive to the phase-parameters than the amplitude parameters. The evolution of the parameters verifies further a good convergence and stable performance of the full-waveform inversion approach.

Finally, Figure 6 presents the misfit distribution of the sampled parameters within each SCE optimization step. After the 2nd iteration, a distinctive wedge-shaped distribution can be observed, and the best solution with minimum misfit is obtained as indicated by the red dot. For higher iterations smaller values of the φ and A parameters are being sampled which means that the estimated source wavelet is becoming more accurate. In addition, all other parameters are sampled within smaller ranges, which indicate that the inversion is converging to a stable global solution.

FWI OF EXPERIMENTAL DATA

The novel radius estimation approach using the FWI was tested for a water-filled plastic pipe measured with PulseEkko 250MHz GPR at a parking place in Orlando, Florida (28°28'32.0"N 81°27'21.3"W), using a common-offset measurement with source-receiver antenna offset of 0.25 m. Corresponding B-Scan data is shown in Figure 7 a). By analyzing the hyperbola with the ray-based method, we get a rough estimation of the pipe radius being about 21 cm, and a depth of about 1.2 m deep for a relative permittivity of 12.5 (See Table 2). Around the ray-based estimated values, a relatively large search range as listed in (1st row) is used to investigate the stability of the SCE FWI approach. The conductivity range was chosen according to experience and literature values. Similarly to the synthetic case, the starting value of conductivity can be randomly selected since the SCE approach is well sampling the solution space. Here we choose as start value the lower bound of the search range.

Figure 7 b) shows that the initial modeled data (blue lines) is not consistent with the measured data (black lines) and shows an apparent waveform shift of indicating an incorrect travel time, which results in a relatively high misfit value of 1.27 (see Figure 7 c). The finally obtained modeled data (red dash lines) are very similar to the measured data and the decrease of the misfit indicates an improved inversion result.

The evolution of the parameters and the misfit distribution versus sampled parameters within the SCE optimization step are illustrated in Figure 8 and Figure 9, respectively. The evolution of parameters during the inversion of measured data contains slightly more fluctuation, and the wedge-shaped misfit distribution versus sampled parameters is similar to the synthetic

data. Table 2 shows the finally obtained inversion result, that returns a radius of 26 cm a depth of 1.2 m.

To investigate the stability of the inversion result, we performed additional tests with start radii of 15.0 cm, 20.0 cm, 25.0 cm, 30.0 cm, and 35 cm while keeping the other parameters fixed. The obtained radii are 28.12 cm, 28.19 cm, 26.99 cm, 23.65 cm, and 23.09 cm, respectively, with an average value of 26.01 cm. Although the range of starting radii was large, the FWI returned radii that were present in a smaller range indicating a radius of 26 cm plus/minus 2-3 cm (see all obtained medium properties in Table 3). Because the inversion results shown in Table 2 returned the smallest misfit of 0.105, we regard this as the optimum inversion result. Note that the inversion result is similar to the mean value of all inversion results obtained by using different starting models, whereas these results are significantly different compared to the ray-based radius estimation of 21 cm.

To verify the stability of the inverted unrealistic high conductivity values, we performed an additional inversion with start conductivity of 20 mS/m, while keeping the other start model unchanged. A comparable conductivity of 55.44 mS/m was obtained, and corresponding relative permittivity, radius, and depth values of 13.43, 26.94 cm and 1.23 m were obtained, respectively. It can be seen that with a different conductivity start model, the inversion still convergences to a result that is comparable to the former results as presented in the Table II. The independency of the start model is due to the solution space being well-sampled by the SCE, as indicated by Figures 6 and Figure 9.

The unrealistic high conductivity (57 mS/m) values are probably due to the use of a point source dipole antenna in the forward model, whereas in reality shielded bowtie antennae are used

that probably have different radiation characteristics (Giannakis et al., 2016). More research needs to be carried out to implement a more detailed antenna model in gprMax which can be easily implemented in the presented approach (Warren and Giannopoulos, 2011). It is expected that in this way real data inversions can be improved and will become more stable and reliable.

CONCLUSION AND OUTLOOK

This work describes a novel approach to estimate the radius of subsurface cylindrical objects as well as the medium's properties and the effective source wavelet using a full-waveform inversion technique, where SCE is used to find the optimum medium properties and an effective source wavelet that explains best the measured data using the 3D FDTD forward modeling tool gprMax. The FWI implementation is based on a combined iterative sequential inversion of the phase parameter of the effective source, the depth, radius, and permittivity followed by the optimization of the amplitude of the effective source wavelet and the conductivity properties. After several iterations of this sequential inversion, a simultaneous permittivity and conductivity optimization is performed by keeping the source wavelet fixed.

By using a combined sequential and simultaneous FWI approach, we can reliably reconstruct the properties of subsurface cylindrical objects from surface GPR data. The tests with synthetic data have shown that the model parameters including source wavelet can be reliably reconstructed. Inversion of the experimental data using a wide range of start model returned medium properties that were well able to explain the measured data, indicating the validity and stability of the new approach. The inversion with the smallest misfit returned a radius of 26 cm whereas the other inversion results indicated an uncertainty of about 2~3 cm. Note that these results are significantly different compared to the ray-based radius estimation of 21 cm.

The inversion of real data is assuming that the pipe is present in a homogeneous medium, whereas in reality it is present in a more complicated medium environment. Improvements are expected by introducing a more representative subsurface that can be layered or include changing medium properties. The unrealistically high electrical conductivity estimations indicate that a more advanced antenna model including shielding will improve the inversion results. Future work consists of including detailed GPR antennas as described by Warren and Giannopoulos in the work of creating FDTD models of commercial GPR antennas.

The combination of gprMax3D and the simultaneous full-waveform inversion of the medium properties and the effective source wavelet makes the presented approach versatile and applicable for a wide range of applications.

ACKNOWLEDGMENTS

The financial support from China Scholarship Council (Project No. 201503170299) and National Natural Science Foundation of China (Grant No. 61372160) are acknowledged. We gratefully acknowledge Peter Annan (Sensors & Software) for providing the measured data, and the developers of gprMax3D for the technical support. Further, we gratefully acknowledge the computing time granted on the supercomputer JURECA at Jülich Supercomputing Centre (JSC). We thank Sebastian Busch and an anonymous reviewer for their help in improving the manuscript.

REFERENCES

Annan, A. P., N. Diamanti, J. D. Redman, and S. R. Jackson, 2016, Ground-penetrating radar for assessing winter roads: Geophysics, **81**, A101-A109.

Babcock, E., and J. H. Bradford, 2015, Reflection waveform inversion of ground-penetrating radar data for characterizing thin and ultrathin layers of nonaqueous phase liquid contaminants in stratified media: Geophysics, **80**, H1-H11.

Borgioli, G., L. Capineri, P. Falorni, S. Matucci, and C. G. Windsor, 2008, The Detection of Buried Pipes From Time-of-Flight Radar Data: IEEE Transactions on Geoscience and Remote Sensing, **46**, 2254-2266.

Bradford, J. H., E. L. Babcock, H. Marshall, and D. F. Dickins, 2016, Targeted reflection-waveform inversion of experimental ground-penetrating radar data for quantification of oil spills under sea ice: Geophysics, **81**, A59-A70.

Busch, S., J. van der Kruk, J. Bikowski, and H. Vereecken, 2012, Quantitative conductivity and permittivity estimation using full-waveform inversion of on-ground GPR data: Geophysics, **77**, H79-H91.

Busch, S., J. van der Kruk, and H. Vereecken, 2014, Improved Characterization of Fine-Texture Soils Using On-Ground GPR Full-Waveform Inversion: IEEE Transactions on Geoscience and Remote Sensing, **52**, 3947-3958.

Caorsi, S., and G. Cevini, 2005, An Electromagnetic Approach Based on Neural Networks for the GPR Investigation of Buried Cylinders: IEEE Geoscience and Remote Sensing Letters, **2**, 3-7.

Cordua, K. S., T. M. Hansen, and K. Mosegaard, 2012, Monte Carlo full-waveform inversion of crosshole GPR data using multiple-point geostatistical a priori information: Geophysics, **77**, H19-H31.

Dérobert, X., J. Iaquinta, G. Klysz, and J. Balayssac, 2008, Use of capacitive and GPR techniques for the non-destructive evaluation of cover concrete: NDT & E International, **41**, 44-52.

Duan, Q. Y., V. K. Gupta, and S. Sorooshian, 1993, Shuffled complex evolution approach for effective and efficient global minimization: Journal of Optimization Theory and Applications, **76**, 501-521.

Ernst, J. R., A. G. Green, H. Maurer, and K. Holliger, 2007a, Application of a new 2D time-domain full-waveform inversion scheme to crosshole radar data: Geophysics, **72**, J53-J64.

Ernst, J. R., H. Maurer, A. G. Green, and K. Holliger, 2007b, Full-Waveform Inversion of Crosshole Radar Data Based on 2-D Finite-Difference Time-Domain Solutions of Maxwell's Equations: IEEE Transactions on Geoscience and Remote Sensing, **45**, 2807-2828.

Feng, X., Q. Ren, C. Liu, and X. Zhang, 2017, Joint acoustic full-waveform inversion of crosshole seismic and ground-penetrating radar data in the frequency domain: Geophysics, **82**, H41-H56.

Giannakis, I., A. Giannopoulos, and C. Warren, 2016, A Realistic FDTD Numerical Modeling Framework of Ground Penetrating Radar for Landmine Detection: IEEE Journal of Selected Topics in Applied Earth Observations and Remote Sensing, **9**, 37-51.

Giannopoulos, A., 2005, Modelling ground penetrating radar by GprMax: Construction and Building Materials, **19**, 755-762.

Gloaguen, E., B. Giroux, D. Marcotte, and R. Dimitrakopoulos, 2007, Pseudo-full-waveform inversion of borehole GPR data using stochastic tomography: Geophysics, **72**, J43-J51.

Gueting, N., T. Vienken, A. Klotzsche, J. van der Kruk, J. Vanderborght, J. Caers, H. Vereecken, and A. Englert, 2017, High resolution aquifer characterization using crosshole GPR full‐waveform tomography: Comparison with direct‐push and tracer test data: Water Resources Research, **53**, 49-72.

Hong, S., H. Wiggenhauser, R. Helmerich, B. Dong, P. Dong, and F. Xing, 2017, Long-term monitoring of reinforcement corrosion in concrete using ground penetrating radar: Corrosion Science, **114**, 123-132.

Ihamouten, A., K. Chahine, V. Baltazart, G. Villain, and X. Derobert, 2011, On variants of the frequency power law for the electromagnetic characterization of hydraulic concrete: IEEE Transactions on Instrumentation and Measurement, **60**, 3658-3668.

Jol, H. M., 2008, Ground penetrating radar theory and applications: Elsevier.

Kalogeropoulos, A., J. van der Kruk, J. Hugenschmidt, S. Busch, and K. Merz, 2011, Chlorides and moisture assessment in concrete by GPR full waveform inversion: Near Surface Geophysics, **9**, 277-285.

Kalogeropoulos, A., J. van der Kruk, J. Hugenschmidt, J. Bikowski, and E. Brühwiler, 2013, Full-waveform GPR inversion to assess chloride gradients in concrete: NDT & E International, **57**, 74-84.

Kaur, P., K. J. Dana, F. A. Romero, and N. Gucunski, 2016, Automated GPR Rebar Analysis for Robotic Bridge Deck Evaluation: IEEE Transactions on Cybernetics, **46**, 2265-2276.

Klotzsche, A., J. van der Kruk, G. Meles, and H. Vereecken, 2012, Crosshole GPR full-waveform inversion of waveguides acting as preferential flow paths within aquifer systems: Geophysics, **77**, H57-H62.

Klotzsche, A., J. van der Kruk, J. Bradford, and H. Vereecken, 2014, Detection of spatially limited high-porosity layers using crosshole GPR signal analysis and full-waveform inversion: Water Resources Research, **50**, 6966-6985.

Krause, D., and P. Thörnig, 2016, JURECA: General-purpose supercomputer at Jülich Supercomputing Centre: Journal of large-scale research facilities JLSRF, **2**, A62.

Kuroda, S., M. Takeuchi, and H. J. Kim, 2007, Full-waveform inversion algorithm for interpreting crosshole radar data: A theoretical approach: Geosciences Journal, **11**, 211-217.

Meles, G. A., J. Van der Kruk, S. A. Greenhalgh, J. R. Ernst, H. Maurer, and A. G. Green, 2010, A New Vector Waveform Inversion Algorithm for Simultaneous Updating of Conductivity and Permittivity Parameters From Combination Crosshole/Borehole-to-Surface GPR Data: IEEE Transactions on Geoscience and Remote Sensing, **48**, 3391-3407.

Montoya, T. P., and G. S. Smith, 1996, A study of pulse radiation from several broad-band loaded monopoles: IEEE Transactions on Antennas and Propagation, **44**, 1172-1182.

Pasolli, E., F. Melgani, and M. Donelli, 2009, Automatic Analysis of GPR Images: A Pattern-Recognition Approach: IEEE Transactions on Geoscience and Remote Sensing, **47**, 2206-2217.

Ristic, A. V., D. Petrovacki, and M. Govedarica, 2009, A new method to simultaneously estimate the radius of a cylindrical object and the wave propagation velocity from GPR data: Computers & Geosciences, **35**, 1620-1630.

Sassen, D. S., and M. E. Everett, 2009, 3D polarimetric GPR coherency attributes and full-waveform inversion of transmission data for characterizing fractured rock: Geophysics, **74**, J23-J34.

Sbartaï, Z. M., S. Laurens, J. Balayssac, G. Arliguie, and G. Ballivy, 2006, Ability of the direct wave of radar ground-coupled antenna for NDT of concrete structures: NDT & E International, **39**, 400-407.

Sbartaï, Z., D. Breysse, M. Larget, and J. Balayssac, 2012, Combining NDT techniques for improved evaluation of concrete properties: Cement and Concrete Composites, 34, 725-733.

Schmid, L., J. Schweizer, J. Bradford, and H. Maurer, 2016, A synthetic study to assess the applicability of full-waveform inversion to infer snow stratigraphy from upward-looking ground-penetrating radar data: Geophysics, **81**, A213-A223.

Shihab, S., and W. Al-Nuaimy, 2005, Radius Estimation for Cylindrical Objects Detected by Ground Penetrating Radar: Subsurface Sensing Technologies and Applications, **6**, 151-166.

Soldovieri, F., R. Solimene, L. Lo Monte, M. Bavusi, and A. Loperte, 2011, Sparse Reconstruction From GPR Data With Applications to Rebar Detection: IEEE Transactions on Instrumentation and Measurement, **60**, 1070-1079.

Streich, R., and J. van der Kruk, 2007, Characterizing a GPR antenna system by near-field electric field measurements: Geophysics, **72**, A51-A55.

van der Kruk, J., R. Streich, and M. Grasmueck, Toward True-Amplitude Vector Migration of GPR Data Using Exact Radiation Patterns, *in* R. D. Miller , J. H. Bradford , and K. Holliger, Advances in Near-surface Seismology and Ground-penetrating Radar, 97-116.

Wai-Lok Lai, W., T. Kind, S. Kruschwitz, J. Wöstmann, and H. Wiggenhauser, 2014, Spectral absorption of spatial and temporal ground penetrating radar signals by water in construction materials: NDT & E International, **67**, 55-63.

Warren, C., and A. Giannopoulos, 2011, Creating finite-difference time-domain models of commercial ground-penetrating radar antennas using Taguchi's optimization method: Geophysics, **76**, G37-G47.

Warren, C., A. Giannopoulos, and I. Giannakis, 2016, gprMax: Open source software to simulate electromagnetic wave propagation for Ground Penetrating Radar: Computer Physics Communications, **209**, 163-170.

Windsor, C., L. Capineri, P. Falorni, S. Matucci, and G. Borgioli, 2005, The estimation of buried pipe diameters using ground penetrating radar: Insight-Non-Destructive Testing and Condition Monitoring, **47**, 394-399.

Zanzi, L., and D. Arosio, 2013, Sensitivity and accuracy in rebar diameter measurements from dual-polarized GPR data: Construction and Building Materials, **48**, 1293-1301.

LIST OF FIGURES

Figure 1. Schematic setup of ray paths and measured reflections from a subsurface cylindrical object.

Figure 2. The FWI flowchart demonstrates the combined sequential and simultaneous inversion approach we used to estimate the model and source wavelet parameters. After determining the start model by the ray-based method, we deconvolve the start model's Greens function from the observed data to obtain an initial source wavelet. Steps 3 to 5 describe the sequential optimization of the phase parameters, followed by an updating of the wavelet, and the optimization of the amplitude parameters. In step 6, a source wavelet estimation is performed. Steps 3-6 are performing iteratively until the criterion in step 7 is achieved. Finally, in step 8, a simultaneous optimization of all model parameters is presented.

Figure 3. The radius estimation with the FWI approach uses a) common-offset B-Scan data with a muted direct wave. 6 traces marked by black dash lines starting from 0.0 m to 0.25 m with a step size of 0.05 m indicate the inverted traces. b) presents the zero-offset arrival time calculated with equation (2), wave peaks and troughs of the inverted traces. The traces are normalized and aligned to the maximum peak for better comparison. c) Comparison of synthetic (black), initial modeled (blue), and inverted data (red) in time domain. d) shows the frequency spectrum corresponding to c).

Figure 4. a) shows the evolution of the effective source wavelet. b) shows the misfit for the initial model (left of the vertical black dashed line), sequential inversion as function of

iteration number, and simultaneous inversion (right of the blue dashed line). c) and d) show the misfit as function of the frequency and position for the initial model, the 1st, 2nd,5th, 8th sequential, and final simultaneous optimization.

Figure 5. Evolution of the parameters for the initial model (left of the vertical black dashed line), 8 sequential inversion iterations, and the final simultaneous inversion (right of the blue dashed line). a) and b) illustrate the permittivity and conductivity of surrounding medium, and c) and d) are the radius and center depth of the subsurface cylinder, respectively. e) and f) show the evolution of phase and amplitude factor. The red dash line in each subfigure indicates the true value.

Figure 6. Misfit distribution versus the sampled parameters within the SCE optimization step for the FWI of synthetic data. The sampled parameter in the searching range at 1st, 2nd, 5th and 8th iteration of the sequential optimization step and the final simultaneous optimization are listed. The red dot in each plot indicates the value that was obtained in each iteration. Note that in the final simultaneous optimization, the source wavelet is fixed and the phase and amplitude factor are not included in the inversion.

Figure 7. FWI of the real measured data. a) Common offset profile measured data from Orlando using a 250 MHz PulseEKKO GPR. The green line indicates the hyperbola for the ray-based approach and the red cycle shows the estimated section of the subsurface cylinder. For convenience, the center position of the pipe (marked by cyan dash line at 83.00 m) is shifted to 0. The observed traces and the modeled traces with initial as well as final model parameters and source wavelet are shown in b). c) and d) show the evolution of the misfit and the estimated source wavelet.

Figure 8. Evolution of the model parameters for the measured pipe and the surrounding medium. Similar to Figure 5, a) and b) illustrate the permittivity and conductivity of surrounding medium, and c) and d) are the radius and center depth of the subsurface cylinder, respectively. e) and f) show the evolution of phase and amplitude factor.

Figure 9. Misfit distribution versus the sampled parameters within the SCE optimization step for the FWI of measured data. The sampled parameter in the searching range at 1st, 2nd, 5th and 8th iteration of the sequential optimization step and the final simultaneous optimization are listed.

LIST OF TABLES

Table 1 Real, initial and inverted synthetic model values

Table 2 FWI configuration and inverted result of measured data

Table 3 FWI of measured data with various start model

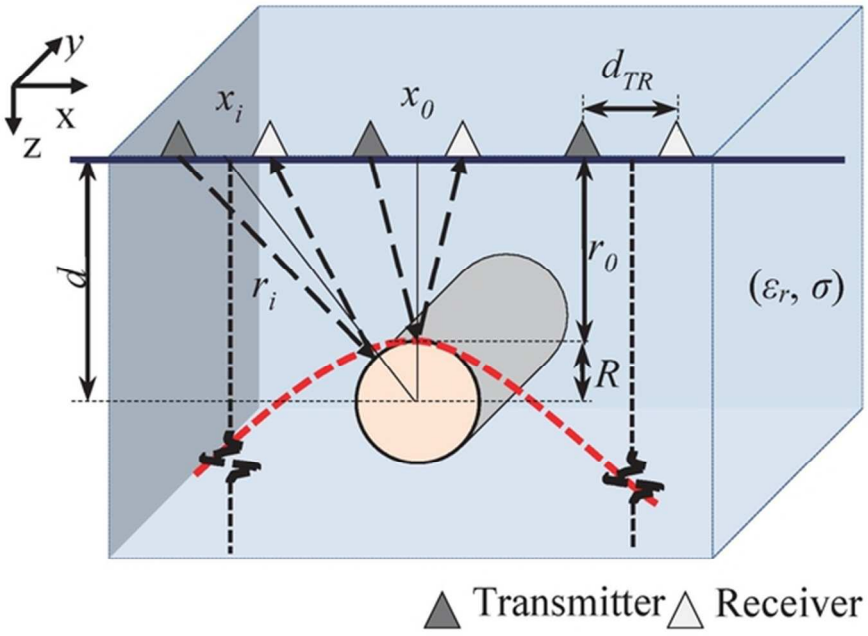

Figure 1. Schematic setup of ray paths and measured reflections from a subsurface cylindrical object.

57x38mm (300 x 300 DPI)

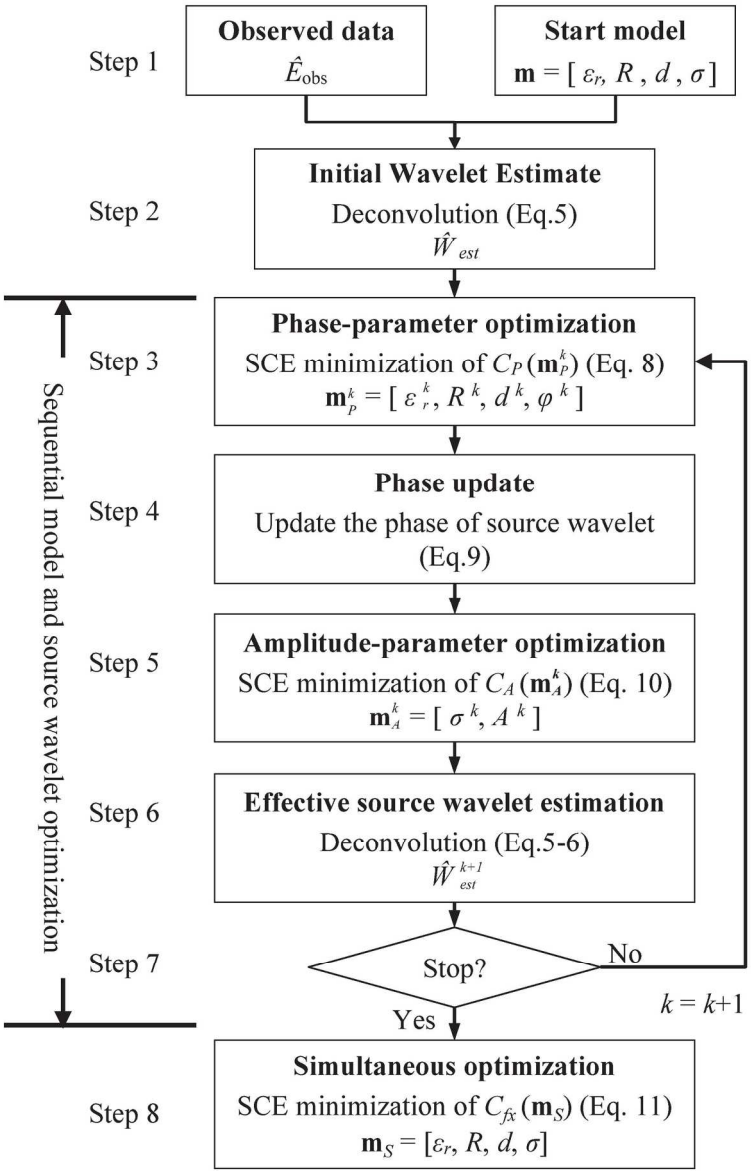

Figure 2. The FWI flowchart demonstrates the combined sequential and simultaneous inversion approach we used to estimate the model and source wavelet parameters. After determining the start model by the ray-based method, we deconvolve the start model's Greens function from the observed data to obtain an initial source wavelet. Steps 3 to 5 describe the sequential optimization of the phase parameters, followed by an updating of the wavelet, and the optimization of the amplitude parameters. In step 6, a source wavelet estimation is performed. Steps 3-6 are performing iteratively until the criterion in step 7 is achieved. Finally, in step 8, a simultaneous optimization of all model parameters is presented.

149x215mm (300 x 300 DPI)

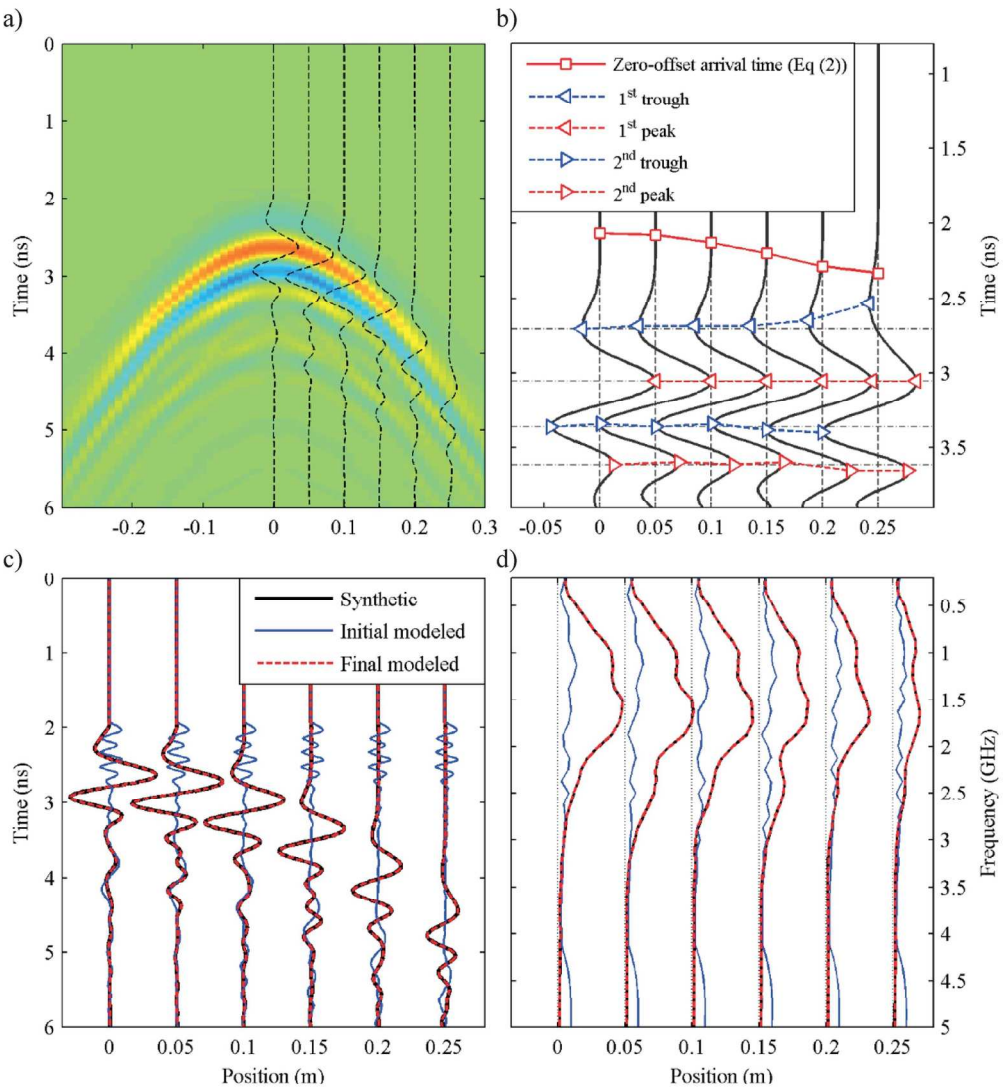

Figure 3. The radius estimation with the FWI approach uses a) common-offset B-Scan data with a muted direct wave. 6 traces marked by black dash lines starting from 0.0 m to 0.25 m with a step size of 0.05 m indicate the inverted traces. b) presents the zero-offset arrival time calculated with equation (2), wave peaks and troughs of the inverted traces. The traces are normalized and aligned to the maximum peak for better comparison. c) Comparison of synthetic (black), initial modeled (blue), and inverted data (red) in time domain. d) shows the frequency spectrum corresponding to c).

149x163mm (300 x 300 DPI)

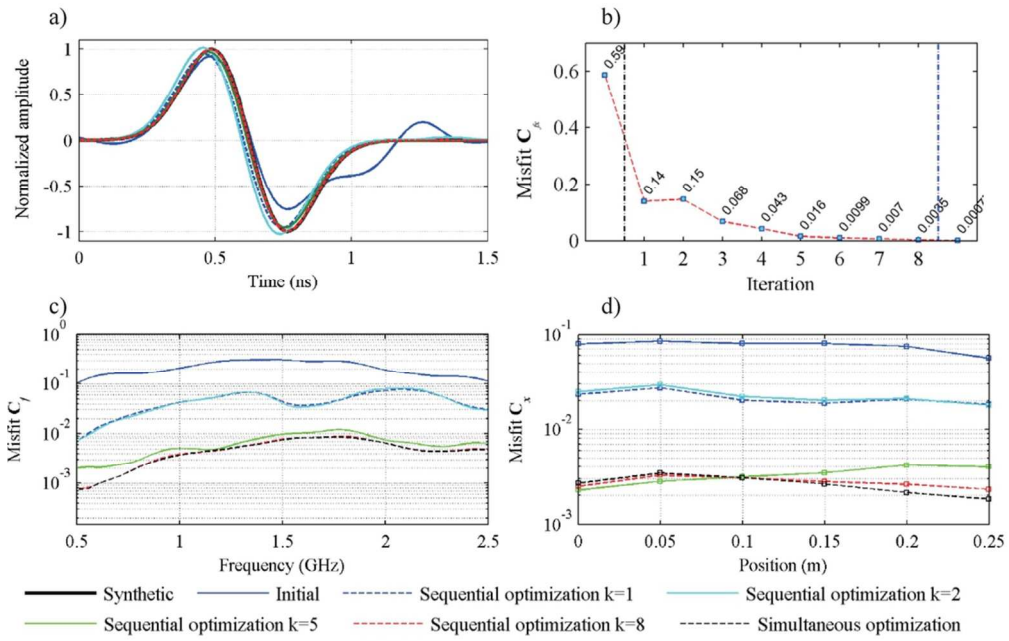

Figure 4. a) shows the evolution of the effective source wavelet. b) shows the misfit for the initial model (left of the vertical black dashed line), sequential inversion as function of iteration number, and simultaneous inversion (right of the blue dashed line). c) and d) show the misfit as function of the frequency and position for the initial model, the 1st, 2nd, 5th, 8th sequential, and final simultaneous optimization.

96x62mm (300 x 300 DPI)

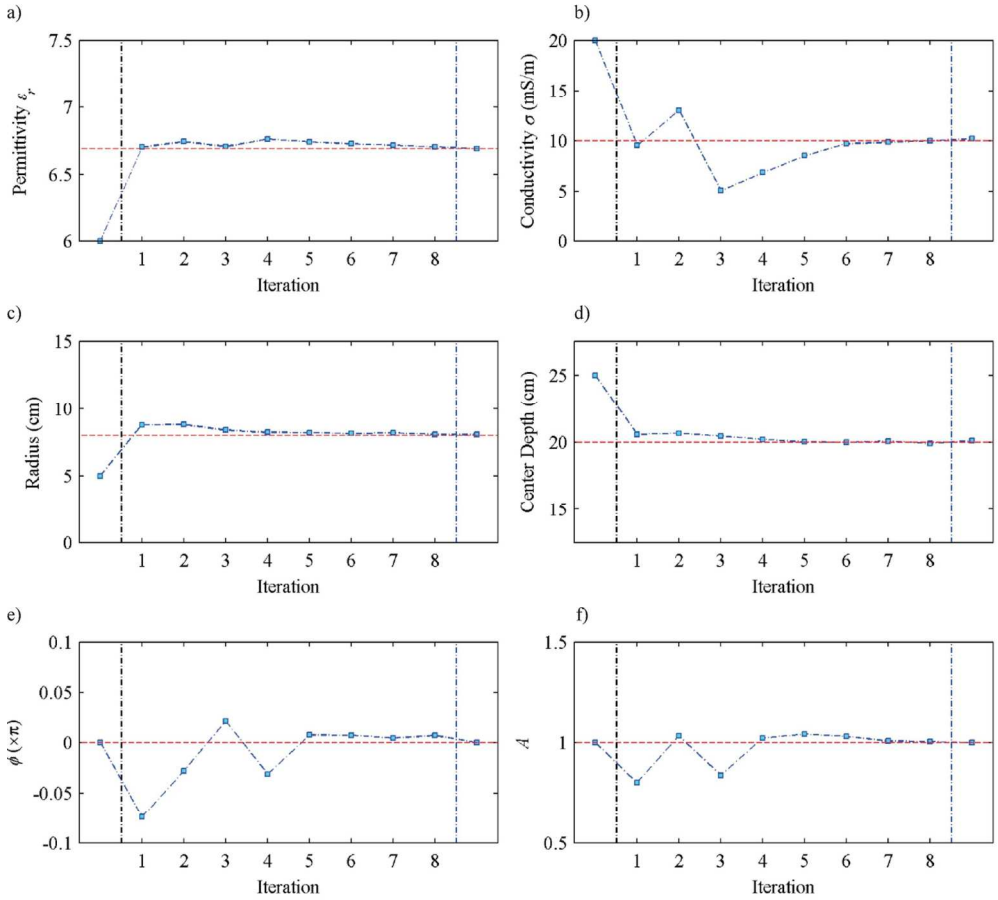

Figure 5. Evolution of the parameters for the initial model (left of the vertical black dashed line), 8 sequential inversion iterations, and the final simultaneous inversion (right of the blue dashed line). a) and b) illustrate the permittivity and conductivity of surrounding medium, and c) and d) are the radius and center depth of the subsurface cylinder, respectively. e) and f) show the evolution of phase and amplitude factor. The red dash line in each subfigure indicates the true value.

137x125mm (300 x 300 DPI)

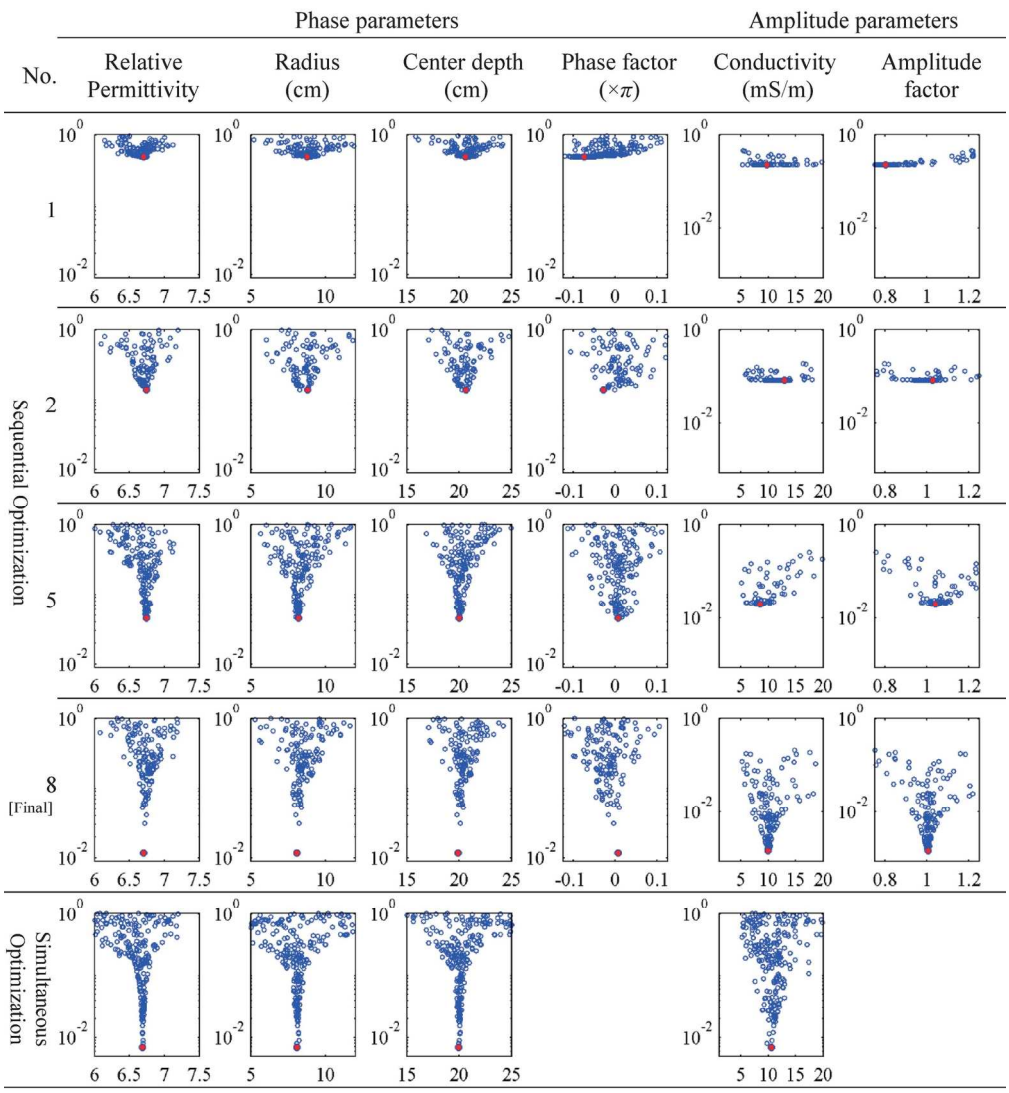

Figure 6. Misfit distribution versus the sampled parameters within the SCE optimization step for the FWI of synthetic data. The sampled parameter in the searching range at 1st, 2nd, 5th and 8th iteration of the sequential optimization step and the final simultaneous optimization are listed. The red dot in each plot indicates the value that was obtained in each iteration. Note that in the final simultaneous optimization, the source wavelet is fixed and the phase and amplitude factor are not included in the inversion.

165x181mm (300 x 300 DPI)

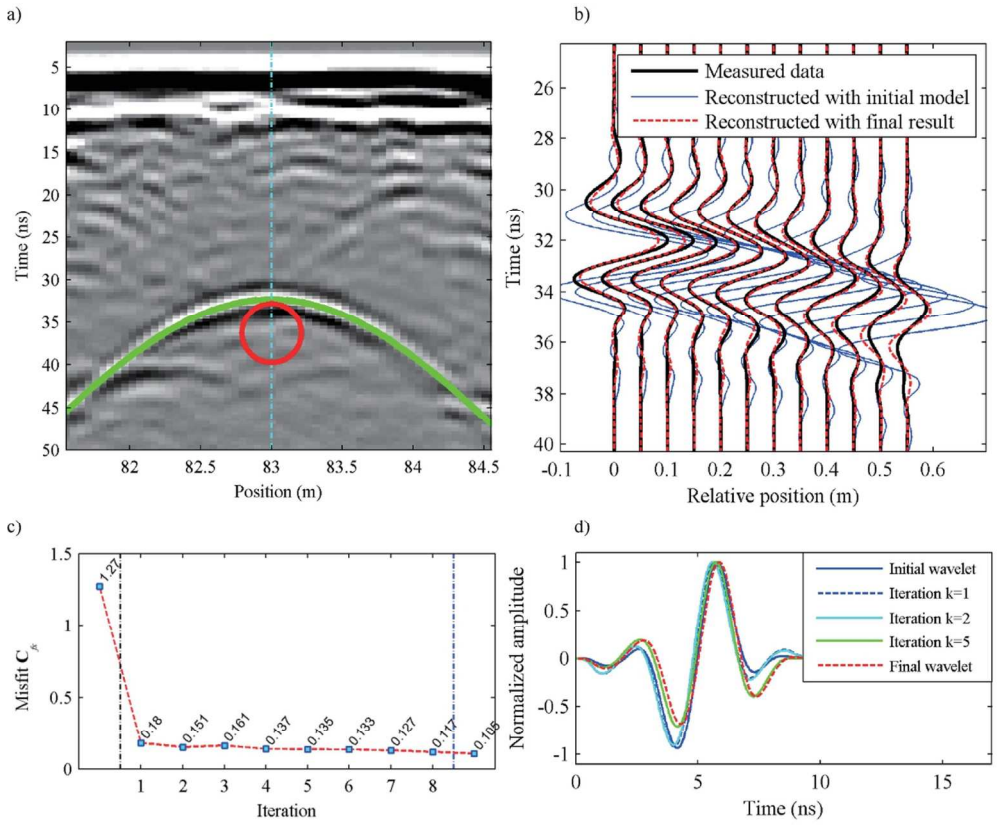

Figure 7. FWI of the real measured data. a) Common offset profile measured data from Orlando using a 250 MHz PulseEKKO GPR. The green line indicates the hyperbola for the ray-based approach and the red cycle shows the estimated section of the subsurface cylinder. For convenience, the center position of the pipe (marked by cyan dash line at 83.00 m) is shifted to 0. The observed traces and the modeled traces with initial as well as final model parameters and source wavelet are shown in b). c) and d) show the evolution of the misfit and the estimated source wavelet.

124x103mm (300 x 300 DPI)

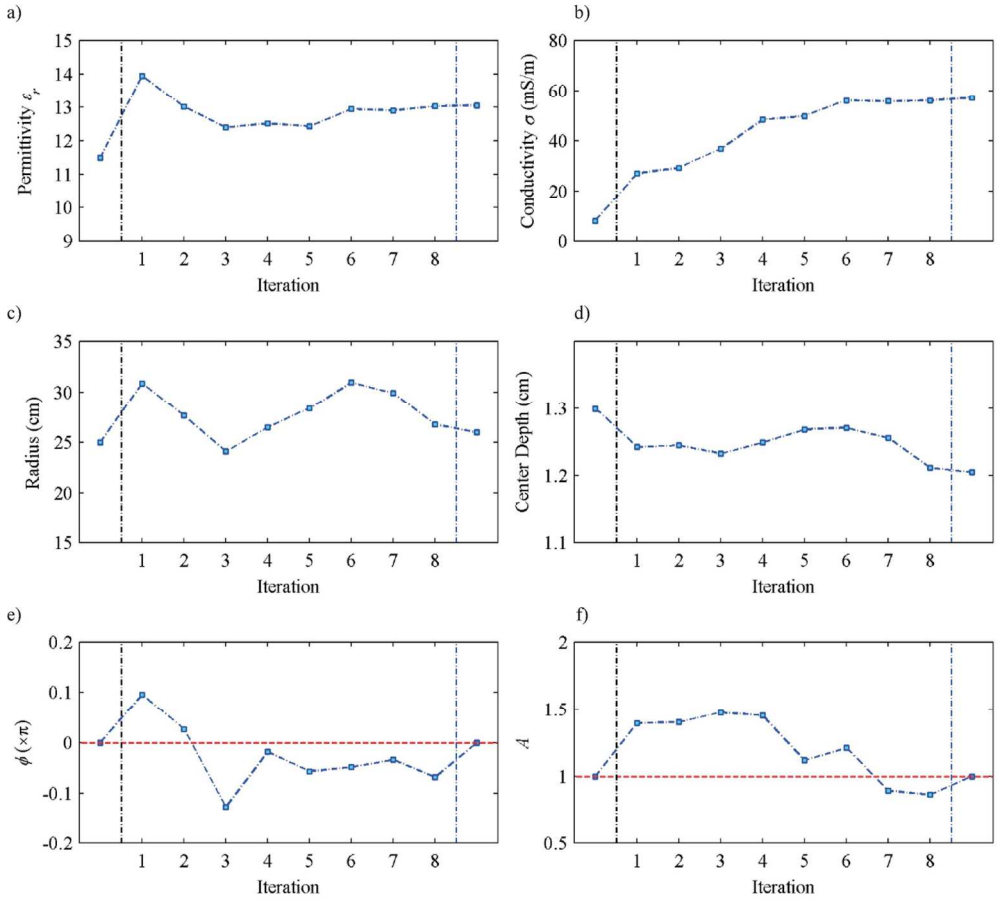

Figure 8. Evolution of the model parameters for the measured pipe and the surrounding medium. Similar to Figure 5, a) and b) illustrate the permittivity and conductivity of surrounding medium, and c) and d) are the radius and center depth of the subsurface cylinder, respectively. e) and f) show the evolution of phase and amplitude factor.

137x125mm (300 x 300 DPI)

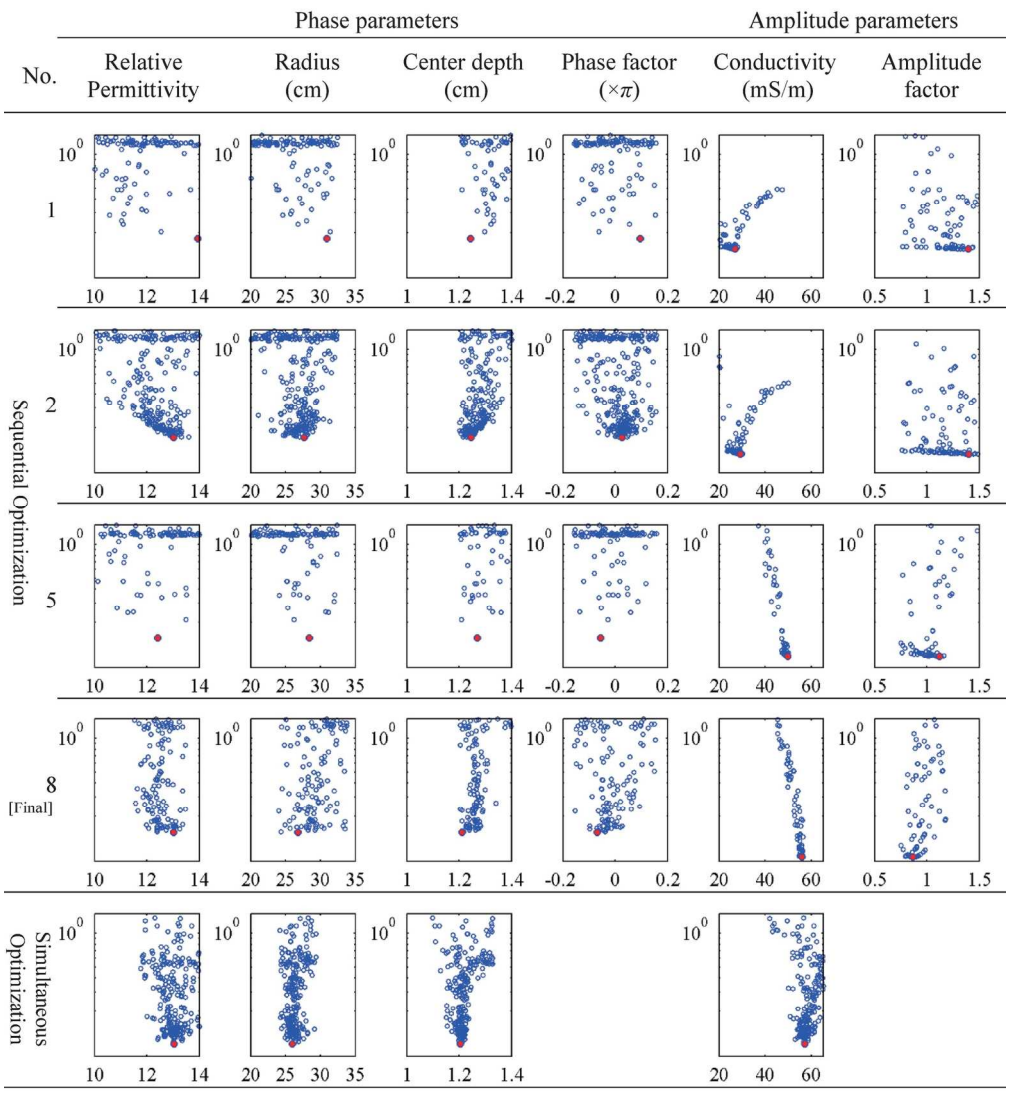

Figure 9. Misfit distribution versus the sampled parameters within the SCE optimization step for the FWI of measured data. The sampled parameter in the searching range at 1st, 2nd, 5th and 8th iteration of the sequential optimization step and the final simultaneous optimization are listed.

165x181mm (300 x 300 DPI)

Table 1

	Medium Properties		Cylinder Geometry		Wavelet	
	Relative Permittivity	Conductivity (mS/m)	Radius (cm)	Center Depth (cm)	φ ($\times\pi$)	A
Real value	6.69	10.00	8.00	20.0	0.0	1.0
Search range	6.00~7.50	5.00~20.00	5.00~12.00	15.0~25.00	-0.1~0.1	0.5~1.5
Start value	6.00	20.00	5.00	25.0	0.0	1.0
Sequential inversion result	6.702	9.99	8.08	19.91	0.0021	1.0043
Simultaneous inversion result	6.689	10.18	8.06	20.09	-	-
Relative error	0.02%	1.80%	0.75%	0.45%	-	-

Table 2

	Medium Properties		Cylinder Geometry		Wavelet	
	Relative Permittivity	Conductivity (mS/m)	Radius (cm)	Center Depth (m)	φ ($\times\pi$)	A
Ray-based estimation	11.50	-	21.0	1.41	-	-
Search range	9.50~14.50	5.00~60.00	15.0~35.0	1.10~1.60	-0.2~0.2	0.5~2.0
Start value	11.50	8.00	25.0	1.30	0.0	1.0
Sequential inversion result	13.02	55.95	26.54	1.21	-0.069	0.83
Simultaneous inversion result	13.05	57.04	25.96	1.21	-	-

Table 3

Start Radius	Relative Permittivity	Conductivity (mS/m)	Radius (cm)	Center Depth (m)	Misfit
15.0	12.96	59.12	28.12	1.31	0.1166
20.0	12.86	57.64	28.19	1.29	0.1225
25.0	13.81	58.85	26.99	1.27	0.1127
30.0	12.72	56.84	23.65	1.27	0.1146
35.0	13.67	51.34	23.09	1.33	0.1173
Average	13.20	56.76	26.01	1.29	0.1167

The start values for permittivity, conductivity and center depth and search range remain same with the value given by Table II.

DATA AND MATERIALS AVAILABILITY

Data associated with this research are available and can be obtained by contacting the corresponding author.